

Flow Visualization of Axisymmetric Steady Marangoni Convection in High-Prandtl-Number Liquid Bridges in Microgravity

Taishi YANO and Koichi NISHINO

Abstract

Microgravity experiments on Marangoni convection in a liquid bridge of high-Prandtl-number fluid so-called *Marangoni Experiment in Space (MEIS)* and *Dynamic Surf (DS)* were performed on board the International Space Station (ISS) to understand the Marangoni convection instability. This study reports the internal flow patterns and velocity profiles of the axisymmetric steady Marangoni convection observed in these projects for various Prandtl numbers ($Pr = 67, 112$ and 207), and for various liquid bridge geometries. The classical three-dimensional particle tracking velocimetry (3-D PTV) is customized for the microgravity experiments, and the spatial structures of the Marangoni convection in liquid bridges are measured with good accuracy. The details of the measurement method currently used, and the results of the 3-D PTV are discussed in this study.

Keyword(s): Marangoni convection, High-Prandtl-number liquid bridge, Axisymmetric steady flow, Three-dimensional particle tracking velocimetry (3-D PTV), International Space Station

Received 4 February 2019, Accepted 15 April 2019, Published 30 April 2019

1. Introduction

Surface tension is caused by the difference between the intermolecular force in the bulk of the liquid below the surface, and that at the surface; this force acts on the liquid to minimize its surface area. Because the intermolecular force is influenced by the temperature, concentration, and electric field, the surface tension is also a function of these factors.^{1,2)} When an inhomogeneous temperature, concentration, or electric charged field exists along the free liquid surface, the difference in surface tension drives the thermocapillary flow, solutocapillary flow, or electrocapillary flow, respectively. These flows are collectively called the Marangoni flow. Since Thomson³⁾ and Marangoni,⁴⁾ who are the pioneering researchers on this phenomenon, investigated the liquid motion driven by a difference of surface tension in the mid-nineteenth century, numerous experimental, theoretical and numerical efforts have been undertaken to date for understanding Marangoni flows. Above all, the Marangoni flow in microgravity (μg , hereafter) has been attracting the special attention of many researchers because surface tension plays an important role under conditions without body force. For example, Marangoni flow occurs during the floating-zone crystal-growth process^{5,6)} in μg , and sometimes the appearance of Marangoni flow affects the quality of the manufactured crystals.⁷⁾

A liquid bridge (LB, hereafter), which is a cylindrical column of liquid connecting rigid parallel disks, is a typical geometry for studying temperature gradient-driven Marangoni convection

(hereafter referred to as Marangoni convection).⁸⁾ Marangoni convection in an LB has been studied in a large number of μg experiments in the sounding rockets, the space shuttles and the space station thus far,⁹⁾ and this study reports on the results of μg experiments conducted on board the International Space Station (ISS). The surface tensions (σ) of many liquids are decreasing functions of the temperature (T); therefore, the liquid at the free surface is driven from warmer regions to cooler regions in this model. **Figure 1** illustrates the flow pattern and the temperature distribution of Marangoni convection in an LB

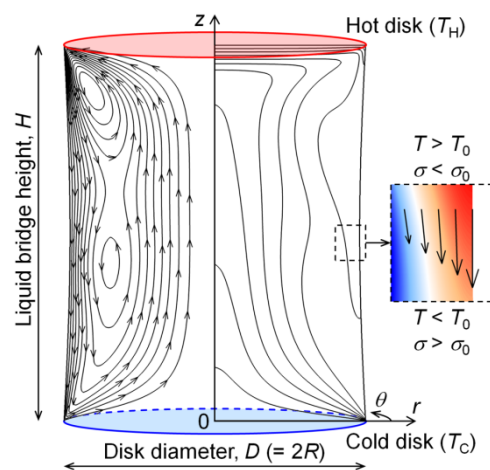


Fig. 1 Temperature gradient-driven Marangoni convection in a liquid bridge. The left and right halves of the diagram represent the streamlines and temperature contours, respectively.

Yokohama National University, 79-5 Tokiwadai, Hodogaya-ku, Yokohama, Kanagawa, 240-8501, Japan.
(E-mail: yano-taishi-gh@ynu.ac.jp)

of high-Prandtl-number fluid under zero-gravity conditions. The data to construct this figure are obtained from a numerical simulation using commercial software STAR-CCM+.¹⁰⁾ Because the lower disk is cooler than the upper disk, the flow is driven from the side of the hot disk (weaker σ side) towards the side of the cold disk (stronger σ side) on the free surface of the LB while transporting the warmer liquid. The liquid arriving at the vicinity of the cold disk changes direction and penetrates into its interior bulk. The liquid then returns to the hot disk side while transporting the cooler liquid to satisfy the principle of the conservation of mass in the LB. However, a part of liquid cannot reach the hot disk and merge with surface flow at the middle height of the LB ($z \approx H/2$), consequently forming two convection rolls: one located near the hot disk and the other in the lower half. The flow pattern with two (or multiple) axially aligned convection rolls rotating in the same direction—the so-called cat's-eye flow²⁾—tends to appear in longer LBs but not in shorter ones. The zone dimension of LB is limited to a short size (say, for heights less than 3 mm) under conditions of normal gravity; therefore, the Marangoni convection in a long LB is an important target of μg experiments.

The remarkable characteristic of Marangoni convection in an LB is the instability. When the temperature difference between the hot disk and the cold disk (i.e., $\Delta T = T_H - T_C$) is increased, the driving force as well as the flow velocity also increases. Marangoni convection in an LB exhibits an axisymmetric steady motion for small ΔT , while it exhibits a non-axisymmetric steady motion or an oscillatory motion for large ΔT .^{11,12)} Such Marangoni instability is strongly affected by the Prandtl number (Pr) of the test liquid; the transition to a non-axisymmetric steady flow occurs in low- Pr cases, and the transition to an oscillatory flow occurs in high- Pr cases. It is reported in the previous theoretical studies^{2,13)} that the former transition is triggered by hydrodynamic instability, while on the other hand, the latter transition is triggered by hydrothermal wave instability. The present study focuses its attention on the Marangoni convection in high- Pr LBs.

The critical conditions for the onset of Marangoni instability in high- Pr LBs have been studied by many researchers, and recent numerical simulations¹⁴⁾ and theoretical stability analyses¹⁵⁾ provide reasonable agreement under critical conditions with the experimental results, meaning that the mechanisms of Marangoni convection instability are progressively revealed.

However, some discrepancies between the results obtained from the experiments and those obtained from the simulations or theories remain. One of the reasons for such discrepancies is the lack of quantitative experimental data that can be used for the validation of numerical simulations and theoretical stability analyses, e.g., data on the velocity and temperature inside the LB, and information on the heat transfer through the LB free surface. It is difficult to measure these quantities using small-scale LBs on Earth under normal gravity, but some of them can be measured using large-scale LBs in μg . The velocity fields inside the LBs have been measured in the μg experiments conducted on board the ISS; this study reports the flow patterns and the velocity profiles of axisymmetric steady Marangoni convection in high- Pr LBs. The results presented here can be used as the benchmark data and can be made available to all researchers working on Marangoni convection.

2. Method

2.1 Experiment

The Japanese Experiment Module Kibo on the ISS has a facility called Fluid Physics Experiment Facility (FPEF), which specializes in Marangoni convection research, and all data presented in this study were obtained in this facility. The μg experiment on Marangoni convection in Kibo consists of four projects: *Marangoni Experiment in Space (MEIS)*, *Dynamic Surf*, *Marangoni UVP*, and *Japanese-European Research Experiment on Marangoni Instability (JEREMI)*; *MEIS*¹⁶⁾ and *Dynamic Surf*¹⁷⁾ were conducted in 2008–2013 and 2013–2016, respectively, *Marangoni UVP* was started in 2010 and is still ongoing, whereas *JEREMI*^{18,19)} is planned for execution in 2020. This study uses the μg experimental data obtained in *MEIS* and *Dynamic Surf*. The details of those projects (e.g., experimental conditions, facility design, procedures) were reported previously,^{16,17)} and only their brief summary is included here.

The projects *MEIS* and *Dynamic Surf* (hereafter referred to as *DS* for brevity) consist of a series of five μg experiments (from *MEIS-1* to *MEIS-5*) and a series of three μg experiments (from *DS-1* to *DS-3*), respectively; the target series in this paper are *MEIS-2*, *MEIS-3*, *MEIS-4*, and *DS-3*. Their time periods of implementation, the supporting disk diameters, and the test liquids are summarized in **Table 1**. The test liquids are silicone oils with the kinematic viscosities of 5, 10 and 20 cSt manufac-

Table 1 Summary of μg experiments targeted in the present study.

	<i>MEIS-2</i>	<i>MEIS-3</i>	<i>MEIS-4</i>	<i>DS-3</i>
Period	Jul. 2009–Aug. 2009	Sep. 2011–Feb. 2012	Aug. 2010–Dec. 2010	Nov. 2015–Nov. 2016
Disk diameter	30 mm	30 mm	50 mm	30 mm
Test liquid	5 cSt silicone oil (KF-96L-5cs)	20 cSt silicone oil (KF-96-20cs)	20 cSt silicone oil (KF-96-20cs)	10 cSt silicone oil (KF-96-10cs)

Table 2 Physical properties of silicone oils at 25°C.

	KF-96L-5cs	KF-96-10cs	KF-96-20cs
Prandtl number, $Pr (= \nu/\alpha)$ [-]	67	112	207
Density, ρ [kg/m ³]	915	935	950
Kinematic viscosity, ν [m ² /s]	5.0×10^{-6}	10.0×10^{-6}	20.0×10^{-6}
Thermal diffusivity, α [m ² /s]	7.46×10^{-8}	8.94×10^{-8}	9.67×10^{-8}
Thermal conductivity, k [W/(m·K)]	0.12	0.14	0.15
Volumetric thermal expansion coefficient, β [1/K]	1.09×10^{-3}	1.06×10^{-3}	1.04×10^{-3}
Surface tension, σ [N/m]	19.7×10^{-3}	20.1×10^{-3}	20.6×10^{-3}
Temperature coefficient of surface tension, σ_T [N/(m·K)]	-6.26×10^{-5}	-6.12×10^{-5}	-5.85×10^{-5} ^(a) -6.24×10^{-5} ^(b)

^(a) MEIS-3 and ^(b) MEIS-4

tured by Shin-Etsu Co., Ltd. (KF-96 series), and their physical properties at 25°C are listed in **Table 2**. We note that the values of σ_T are based on the measurements by Nishino *et al.*¹⁶⁾ and the other values are supplied by the manufacturer.²⁰⁾ The gold-nickel-coated acrylic tracer particles (Soken Chemical & Engineering Co., Ltd.) are seeded into the silicone oils for flow visualization, and their average diameter is approximately 180 μm and average density is approximately 1400 kg/m³. The silicone-oil LB was formed in a gap between the sapphire disk with the temperature of T_H and the aluminum disk with the temperature of T_C . Since the value of T_H is always set to be higher than that of T_C , the sapphire disk and the aluminum disk are hereafter referred to as the hot disk and the cold disk, respectively.

The main measurement devices installed in the FPEF are as follows: (1) three top-view-CCD cameras (from channel 1 to 3) for the three-dimensional particle tracking velocimetry (3-D PTV),²¹⁾ (2) a side-view-CCD camera for the observation of the shape of the LB and its overall flow pattern, (3) an infrared (IR) camera for the measurement of the temperature distribution on the LB free surface, (4) three K-type thermocouple sensors for the measurement of T_C , and (5) two indium tin oxide (ITO) film sensors for the measurement of T_H . Three top-view cameras can observe the motions of tracer particles inside the LB through the

transparent sapphire disk (**Fig. 2**), and the particle images taken from the different view angles are used to determine the spatial motion of each tracer particle in 3-D PTV. This study provides the flow patterns and the velocity profiles of the steady Marangoni convection measured by 3-D PTV, and the details of the data analysis are described in the next section.

2.2 Three-Dimensional Particle Tracking Velocimetry (3-D PTV)

3-D PTV is a simple and effective technique for visualizing complex flow structures. The 3-D PTV measurements of Marangoni convection in an LB have been carried out by several researchers previously.^{21,22)} The data analysis method used in the current 3-D PTV is based on that developed by Nishino *et al.*,²³⁾ but with some important improvements. The main data analysis procedure consists of five steps. The initial step is the camera calibration. The reference points, whose positions in the absolute coordinate system are already known, are marked on the cold disk surface as white dots, and the images of these dots are captured by each top-view camera. The positions of reference points in the image coordinate system (X , Y) and those in the absolute coordinate system (x , y , z) are related to each other by the collinearity condition^{23,24)} as follows:

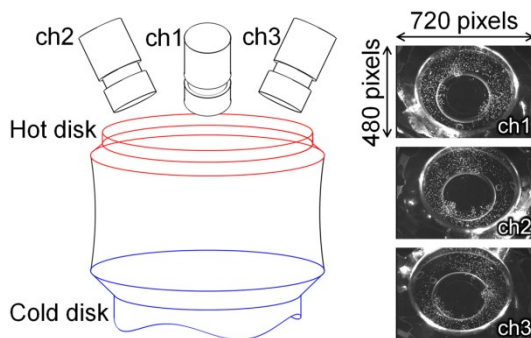


Fig. 2 Schematic image of top-view-CCD cameras and their captured images.

$$X/A_{\text{pixel}} = -c \frac{a_{11}(x-x_0) + a_{12}(y-y_0) + a_{13}(z-z_0)}{a_{31}(x-x_0) + a_{32}(y-y_0) + a_{33}(z-z_0)} + \Delta X, \quad (1a)$$

$$Y = -c \frac{a_{21}(x-x_0) + a_{22}(y-y_0) + a_{23}(z-z_0)}{a_{31}(x-x_0) + a_{32}(y-y_0) + a_{33}(z-z_0)} + \Delta Y, \quad (1b)$$

$$a_{ij} = \begin{bmatrix} 1 & 0 & 0 \\ 0 & \cos \omega & -\sin \omega \\ 0 & \sin \omega & \cos \omega \end{bmatrix} \begin{bmatrix} \cos \phi & 0 & \sin \phi \\ 0 & 1 & 0 \\ -\sin \phi & 0 & \cos \phi \end{bmatrix} \begin{bmatrix} \cos \kappa & -\sin \kappa & 0 \\ \sin \kappa & \cos \kappa & 0 \\ 0 & 0 & 1 \end{bmatrix}, \quad (2)$$

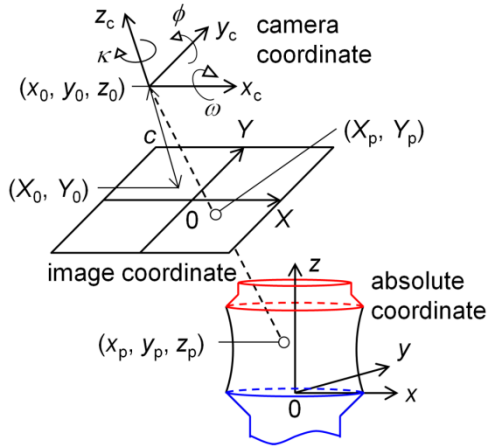


Fig. 3 Relationship between the absolute coordinate system and the image coordinate system under conditions of collinearity.

$$\begin{aligned} \Delta X &= X_0 + (X/A_{\text{pixel}} - X_0)(k_1 r^2 + k_2 r^4) \\ &\quad + p_1 \{r^2 + 2(X/A_{\text{pixel}} - X_0)\} + 2p_2 (X/A_{\text{pixel}} - X_0)(Y - Y_0), \end{aligned} \quad (3a)$$

$$\begin{aligned} \Delta Y &= Y_0 + (Y - Y_0)(k_1 r^2 + k_2 r^4) \\ &\quad + 2p_1 (X/A_{\text{pixel}} - X_0)(Y - Y_0) + p_2 \{r^2 + 2(Y - Y_0)\}, \end{aligned} \quad (3b)$$

$$r = \sqrt{\frac{(X/A_{\text{pixel}} - X_0)^2 + (Y - Y_0)^2}{c^2}}. \quad (4)$$

These equations include 14 camera parameters, where (x_0, y_0, z_0) are the absolute coordinates of the view point, (ω, ϕ, κ) are the rotation angles of the camera, c is the principal distance, (X_0, Y_0) are the shifts of the principal point, (k_1, k_2) are the radial distortion coefficients, (p_1, p_2) are the decentering distortion coefficients, and A_{pixel} is the pixel aspect ratio (Y to X). The former six parameters are the exterior orientations, and the latter eight parameters are the interior orientations. We note that the origins of the absolute coordinate system and the image coordinate system are defined to be at the centers of the cold disk and the captured image, respectively (**Fig. 3**). The camera parameters are calculated iteratively by the Levenberg-Marquardt method²⁵⁾ using Eqs. (1)–(4) and more than 300 pieces of calibration data. The resultant calibration errors are less than 0.9 pixels for all top-view cameras, which is acceptable for an accurate 3-D PTV.

The second and third steps of the 3-D PTV currently in use are the particle detection and the particle tracking steps. After background subtraction from the original image, tracer particles are detected by the Hough transform method,²⁶⁾ which is effective in finding circles with the diameter greater than 10 pixels. The average diameter of the present tracer particles on the images is approximately 3 to 4 pixels; therefore, the Hough transform method is applied to the image magnified tenfold and

then results are resized to the original magnification. The motions of the detected tracer particles from the first to the second frames are tracked by the use of an algorithm that is the hybrid of the nearest neighbor method and the cross correlation method. The motions of the particles from the second to the third frames are determined by referring to the previous velocities, and the motions after the third frame are determined by referring to the previous velocities and accelerations. These procedures are applied repeatedly to the time-consecutive frames to construct long particle trajectories defined in the image coordinate system.

The fourth step is the 3-D reconstruction. The particle trajectories obtained in the previous step are transformed into the absolute coordinate system by using Eqs. (1)–(4) and the camera parameters. When the target tracer particle is located at $(X, Y) = (X_p, Y_p)$ on the image coordinate system, Eqs. (1a) and (1b) can be written as

$$s_X(x - x_0) + t_X(y - y_0) + u_X(z - z_0) = 0, \quad (5a)$$

$$s_Y(x - x_0) + t_Y(y - y_0) + u_Y(z - z_0) = 0, \quad (5b)$$

respectively, where

$$\begin{cases} s_X = (X_p - \Delta X)a_{31} + ca_{11} \\ t_X = (X_p - \Delta X)a_{32} + ca_{12} \\ u_X = (X_p - \Delta X)a_{33} + ca_{13} \end{cases} \quad \text{and} \quad \begin{cases} s_Y = (Y_p - \Delta Y)a_{31} + ca_{21} \\ t_Y = (Y_p - \Delta Y)a_{32} + ca_{22} \\ u_Y = (Y_p - \Delta Y)a_{33} + ca_{23} \end{cases}.$$

Equations (5a) and (5b) each represent a plane in a 3-D space, and the intersection line of these two planes indicates the perspective ray connecting the tracer particle (x_p, y_p, z_p) and the view point (x_0, y_0, z_0) as follows:

$$\vec{l} = \begin{pmatrix} t_X u_Y - u_X t_Y \\ u_X s_Y - s_X u_Y \\ s_X t_Y - t_X s_Y \end{pmatrix} L + \begin{pmatrix} x_0 \\ y_0 \\ z_0 \end{pmatrix}, \quad (6)$$

where L is the arbitrary constant. The current facility has three top-view cameras, and if these cameras target the same tracer particle, all the perspective rays from the different cameras intersect at the current location of the tracer particle. However, these perspective rays do not strictly converge to an exact point in many cases because of the calibration errors as illustrated in **Fig. 4**. The minimum distance between the perspective rays from two cameras is calculated as

$$d_{\min} = \begin{pmatrix} x_0^{(n)} - x_0^{(m)} \\ y_0^{(n)} - y_0^{(m)} \\ z_0^{(n)} - z_0^{(m)} \end{pmatrix} \cdot \frac{\vec{l}^{(n)} \times \vec{l}^{(m)}}{|\vec{l}^{(n)} \times \vec{l}^{(m)}|}, \quad (7)$$

where super scripts (n) and (m) denote the channel numbers of the camera. If the values of $|d_{\min}|$ for all frames are less than the threshold (i.e., 0.15 mm for $D = 30$ mm and 0.25 mm for $D = 50$ mm in this study), the target tracer particle is reconstructed into

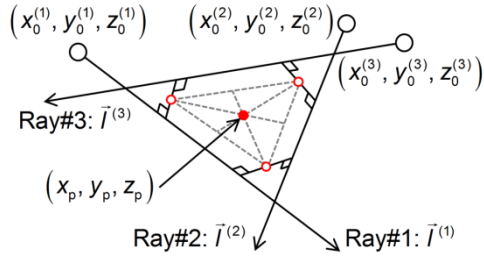


Fig. 4 Positional relationship between the perspective rays from three cameras.

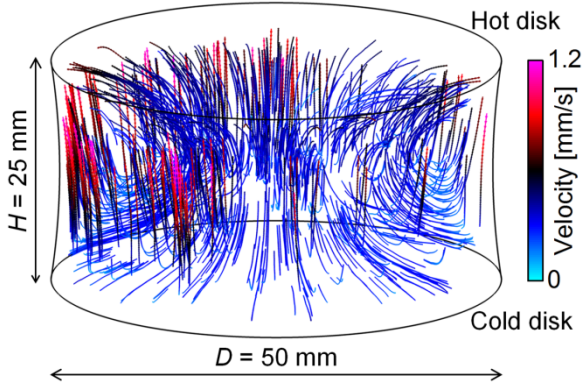


Fig. 5 Particle trajectories of steady Marangoni convection in a liquid bridge visualized by the 3-D PTV, where $Pr = 207$, $A = 0.50$, $V = 0.95$, $T_C = 20.0^\circ\text{C}$, and $T_H = 35.4^\circ\text{C}$ ($\Delta T = 15.4\text{ K}$).

the 3-D space at the middle point of the common normal lines. In the case when the above condition is satisfied for all camera combinations (i.e., ch1 & ch2, ch2 & ch3, and ch3 & ch1), the target tracer particle is reconstructed at the centroid of the triangle formed by the middle points of the common normal lines (**Fig. 4**). In the present study, the particle trajectories tracked over 30 frames are used to find the corresponding particle trajectory in the different camera; therefore, the number of erroneous vectors is comparatively smaller than the previous 3-D PTV in which the matching of the tracer particles was done for each single frame.

The final step is error reduction. The particle tracking and 3-

D reconstruction methods presently used can improve the accuracy of 3-D PTV; however, some erroneous vectors may survive due to calibration errors or other reasons. These erroneous vectors are often located outside the measurement volume or are observed to exhibit obviously strange motions, and they are discarded. **Figure 5** shows the particle trajectories of steady Marangoni convection in an LB obtained by the present 3-D PTV, where the particle trajectories reconstructed by three cameras and those reconstructed by two cameras are shown together. The toroidal flow pattern can be recognized, and this result qualitatively indicates the validity of the present 3-D PTV.

3. Results and Discussion

3.1 Flow fields for $A = 0.50$

The flow patterns of Marangoni convection in high- Pr LBs for $A = 0.50$ and $T_C = 20^\circ\text{C}$ are shown in **Fig. 6**, where experimental conditions are listed in **Table 3**. We note that A ($= H/D$) is the aspect ratio (i.e., the ratio of LB height H to the disk diameter D), V ($= V_{LB}/\pi R^2 H$) is the volume ratio (i.e., the ratio of LB volume V_{LB} to the gap volume between supporting disks $\pi R^2 H$), Ma is the Marangoni number, and U is the characteristic velocity.²⁾ The Marangoni number represents the intensity of convection, and it is defined as

$$Ma = \frac{|\sigma_T| \Delta T R}{\rho \bar{\nu} \alpha}, \quad (8)$$

where R ($= D/2$) is the disk radius and $\bar{\nu}$ is the mean of ν at T_C and T_H . We note that R is chosen as the characteristic length because it becomes more relevant for longer LBs as pointed out by Nishino *et al.*¹⁶⁾ The following equation²⁰⁾ is used to evaluate ν at an arbitrary temperature T [$^\circ\text{C}$]:

$$\nu(T) = \nu(25^\circ\text{C}) \times \exp\left(5.892 \times \frac{25 - T}{273.15 + T}\right). \quad (9)$$

The characteristic velocity is defined as

$$U = \frac{|\sigma_T| \Delta T}{\rho \bar{\nu}}. \quad (10)$$

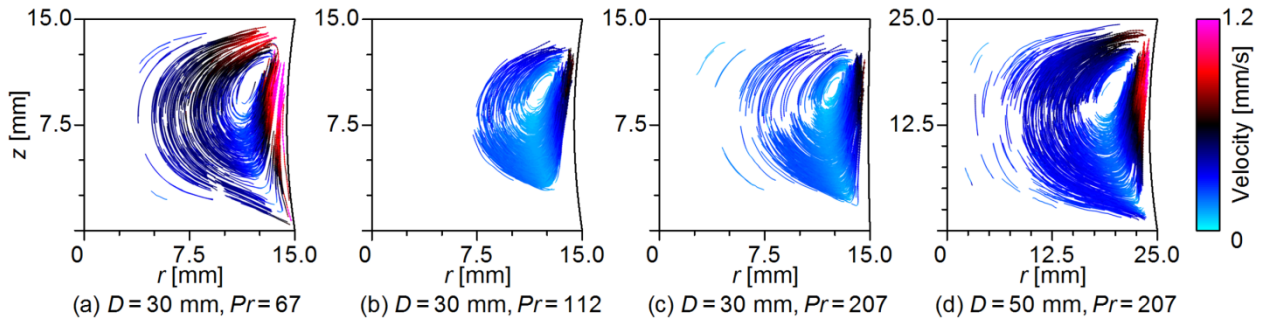


Fig. 6 Particle trajectories obtained by 3-D PTV for $A = 0.50$: (a) MEIS-2, (b) DS-3, (c) MEIS-3, and (d) MEIS-4. The experimental conditions are listed in **Table 3**.

Table 3 Experimental conditions of 3-D PTV for $A = 0.50$ shown in Fig. 6.

	Series	ΔT [K] ($\Delta T/\Delta T_c$ [-])	Ma [-]	U [mm/s]	V [-]
a	MEIS-2	7.2 (0.96)	1.9×10^4	94.7	0.95
b	DS-3	13.6 (0.95)	1.5×10^4	91.5	0.95
c	MEIS-3	23.9 (0.82)	1.3×10^4	81.4	0.99
d	MEIS-4	15.4 (0.92)	1.4×10^4	52.5	0.95

The instability thresholds of Marangoni convection in high- Pr LBs in MEIS and DS (i.e., Ma at critical temperature difference ΔT_c) were reported by Nishino *et al.*¹⁶⁾ and Yano *et al.*¹⁷⁾, respectively. Since the values of ΔT considered in this study are lower than its critical boundary, the flow states are subcritical and the flow fields exhibit axisymmetric steady motions. Therefore, the particle trajectories located at different azimuthal angles θ (see Fig. 1) are superposed onto the same azimuthal cross plane in each of the Figs. 6(a)–6(d). It is important to mention that the numbers of tracer particles seeded into the silicone oil in MEIS-3 and DS-3 are considerably larger than those in MEIS-2 and MEIS-4 (approximately four-fold), resulting in the overclouded particle images and the small numbers of reconstructed particle trajectories in Figs. 6(b) and 6(c). All results presented in Fig. 6 indicate a single toroidal convection roll rotating in a clockwise direction, and each center of convection roll is located near the hot corner from where the surface flow primarily originates. The velocity profiles of radial (u_r) and axial (u_z) components along the z direction at $r/R = 0.50$ (return flow) and 0.95 (surface flow) are compared quantitatively in

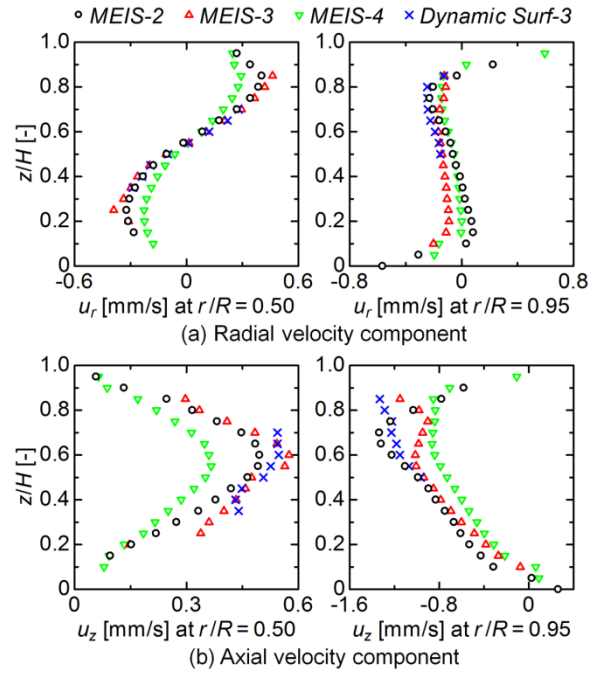

Fig. 7 Velocity profiles along the z direction at $r/R = 0.5$ (left) and 0.95 (right) for $A = 0.50$: (a) radial component, and (b) axial component.

Fig. 7, where the mean velocities inside the $0.04D \times 0.04D$ square regions (1.2×1.2 mm² for $D = 30$ mm and 2.0×2.0 mm² for $D = 50$ mm) are plotted as a function of z/H . We note that the typical measurement uncertainties of u_r and u_z are ± 0.05 mm/s and ± 0.11 mm/s, respectively, where those values are evaluated from the standard deviations. The results indicate a

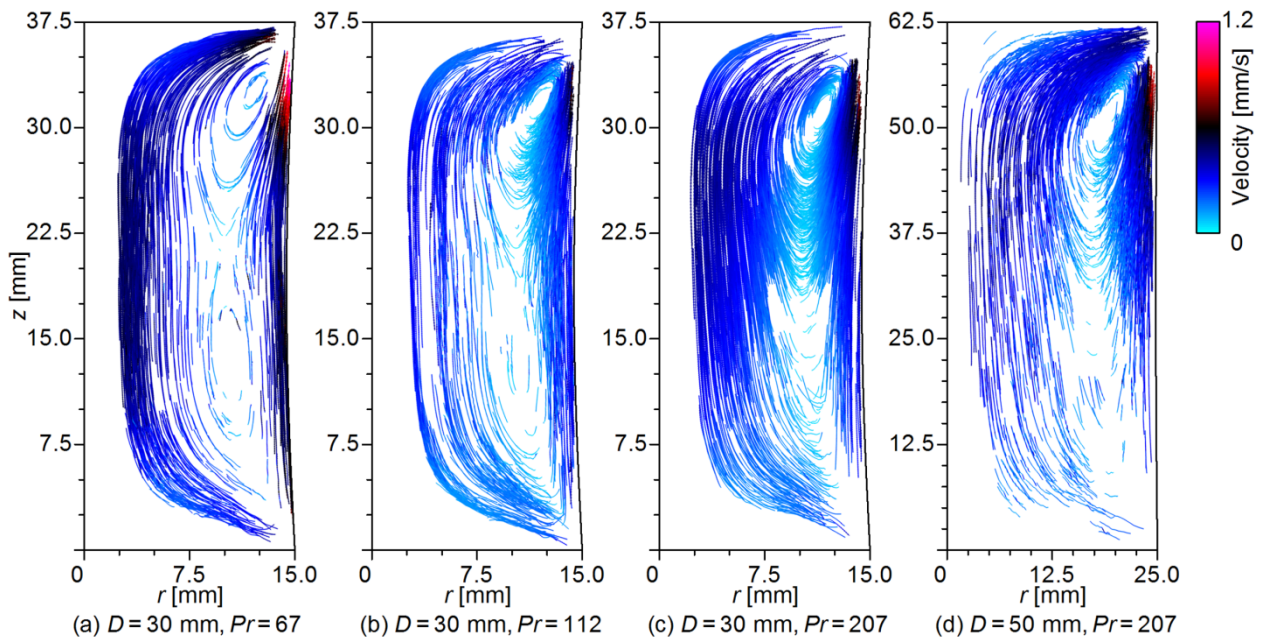

Fig. 8 Particle trajectories obtained by 3-D PTV for $A = 1.25$: (a) MEIS-2, (b) DS-3, (c) MEIS-3, and (d) MEIS-4. The experimental conditions are listed in Table 4.

Table 4 Experimental conditions of 3-D PTV for $A = 1.25$ shown in **Fig. 8**.

	Series	ΔT [K] ($\Delta T/\Delta T_c$ [-])	Ma [-]	U [mm/s]	V [-]
a	MEIS-2	4.5 (0.83)	1.2×10^4	57.6	0.95
b	DS-3	7.0 (0.66)	7×10^3	44.4	0.95
c	MEIS-3	15.3 (0.86)	8×10^3	48.7	0.95
d	MEIS-4	8.8 (0.92)	7×10^3	26.6	0.99

similar trend in both the radial and axial velocity profiles, but their magnitudes are different depending on D . As shown in **Table 3**, the characteristic velocity for $D = 50$ mm is lower than that for $D = 30$ mm, and this difference is reflected in the difference in the velocity magnitude shown in **Fig. 7**.

3.2 Flow fields for $A = 1.25$

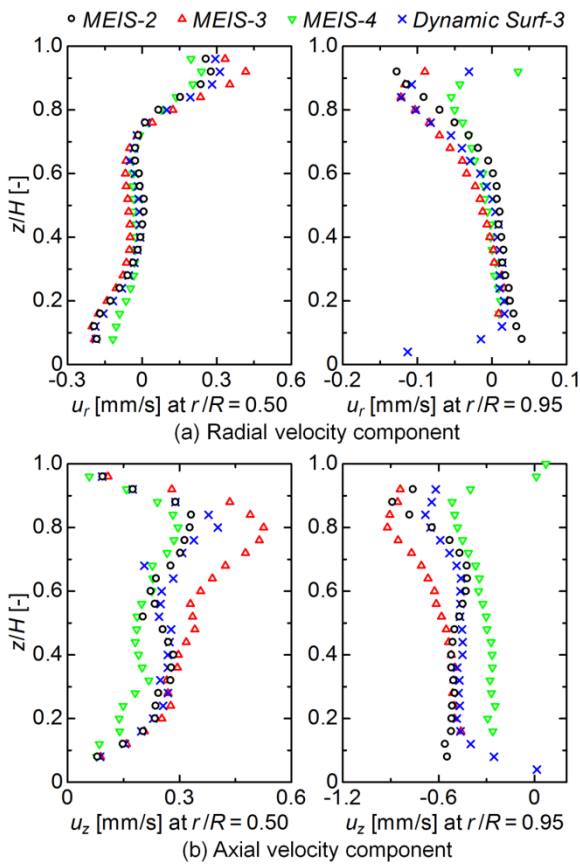
The particle trajectories measured by 3-D PTV for $A = 1.25$ and $T_c = 20^\circ\text{C}$ are shown in **Fig. 8**, where experimental conditions are listed in **Table 4**. Since the flow states are also sub-critical, the particle trajectories are plotted onto the same azimuthal cross plane. In contrast to the results for $A = 0.50$, the particle trajectories for $A = 1.25$ indicate different flow patterns

depending on the test liquid. For $Pr = 67$ (**Fig. 8(a)**), two convection rolls both rotating in the clockwise direction can be recognized: one located near the hot disk and the other located near the cold disk, and the sizes of these convection rolls seem to be comparable. For $Pr = 112$ (**Fig. 8(b)**), the particle trajectories also exhibit two convection rolls; however, the size of the convection roll near the hot disk expands and that near the cold disk shrinks. For $Pr = 207$ (**Figs. 8(c)** and **8(d)**), the convection roll near the hot disk occupies the entire flow field inside the LB and the secondary convection roll cannot be recognized.

The velocity profiles of u_r and u_z along the z direction at $r/R = 0.50$ (return flow) and 0.95 (surface flow) are presented in **Fig. 9**, where the mean velocities are determined by the same way as with **Fig. 7**. The typical measurement uncertainties of u_r and u_z are ± 0.02 mm/s and ± 0.06 mm/s, respectively. Since the value of U for $D = 50$ mm is smaller than that for $D = 30$ mm as indicated in **Table 4**, the velocity magnitudes, especially the axial component, for $D = 50$ mm are smaller than those for $D = 30$ mm. In **Fig. 9(b)**, the results for $D = 30$ mm show a different trend in the axial velocity profile depending on Pr , in that the magnitudes of both return flow and surface flow velocities for $Pr = 207$ are larger than those for $Pr = 67$ and 112 in the upper half region of the LB (i.e., $0.5 \leq z/H \leq 1.0$). Such differences in the flow velocity seem to be reflected in the differences in the flow pattern (**Fig. 8**). It is important to mention that the changes in the basic flow pattern and flow velocity recognized in **Figs. 8** and **9** are not only caused by the effect of Pr , but may be due to the effect of heat transfer at the LB free surface. Melnikov *et al.*¹⁴⁾ and Shitomi *et al.*²⁷⁾ reported the significant effect of interfacial heat transfer on the basic flow pattern of Marangoni convection in high- Pr LBs. Further, they demonstrated the enhancement of the convection roll near the hot disk due to the increase of heat loss from the LB free surface in their numerical simulations. Since the heat loss from the LB free surface increases with increasing ΔT , the LB with $Pr = 207$ is cooled more heavily than the other cases, and the larger heat loss changes the basic flow pattern and the flow velocity.

4. Conclusions

This paper reports the details of the three-dimensional particle tracking velocimetry (3-D PTV) adopted in the microgravity (μg) experiments on Marangoni convection in a liquid bridge (LB) and the results of flow measurements of axisymmetric steady Marangoni convection by 3-D PTV. Two projects of μg experiments called *Marangoni Experiment in Space (MEIS)* and *Dynamic Surf* have been conducted on the Japanese Experiment Module Kibo on the International Space Station for understanding the instability mechanisms of Marangoni convection in high-Prandtl-number LBs. A silicone-oil LB with the Prandtl number of $Pr = 67, 112, \text{ or } 207$ is formed between the differen-

**Fig. 9** Velocity profiles along the z direction at $r/R = 0.50$ (left) and 0.95 (right) for $A = 1.25$: (a) radial component, and (b) axial component.

tially heated supporting disks in these projects. The temperature difference ΔT between those disks drives the Marangoni convection, while the target flow state in this study is an axisymmetric and steady. The classical 3-D PTV is optimized for better measurement of Marangoni convection under μg condition, which allows one to obtain the velocity fields inside the LBs with acceptable accuracy. The 3-D PTV measurements are performed to visualize Marangoni convection in short ($A = 0.50$) and long ($A = 1.25$) LBs, where $A (= H/D)$ is the ratio of the LB height H to the disk diameter D . The measurement results of flow velocities indicate that the Marangoni convection in LBs with larger diameter (i.e., $D = 50$ mm) moves more slowly than that in LBs with smaller diameter (i.e., $D = 30$ mm). The measurement results of flow patterns for $A = 0.50$ exhibit a similar single convection roll regardless of Pr . On the other hand, the results for $A = 1.25$ exhibit different flow patterns depending on Pr . Two axially aligned convection rolls are recognized for $Pr = 67$ and 112, while a single convection roll occupies the entire flow field inside the LB for $Pr = 207$. Such a change of flow pattern is considered to be caused by the effect of heat transfer through the LB free surface.

Acknowledgments

The authors greatly appreciate Prof. Hiroshi Kawamura (Suwa University of Science, Japan), Prof. Yasuhiro Kamotani (Case Western Reserve University, USA), Prof. Ichiro Ueno (Tokyo University of Science, Japan), Prof. Atsuki Komiya (Tohoku University, Japan), Prof. Nobuyuki Imaishi (Kyushu University, Japan), Dr. Satoshi Matsumoto, Dr. Mitsuru Ohnishi and Dr. Masato Sakurai (Japan Aerospace Exploration Agency, Japan), and all other members of the *MEIS* and *Dynamic Surf* projects for their contributions to the μg experiments. The author KN acknowledges the financial support by the Japan Society for the Promotion of Science (JSPS) KAKENHI (Grant-in-Aid for Scientific Research (C), No. 17K06190).

References

- 1) D.C. Grahame: Chem. Rev., **41** (1947) 441.
- 2) H.C. Kuhlmann: Thermocapillary Convection in Models of Crystal Growth. Springer Tracts in Modern Physics 152, Springer, Berlin, Heidelberg, 1999.
- 3) J. Tomson: Philos. Mag. Ser. **4**, 10 (1855) 330.
- 4) C. Marangoni: Ann. Phys. Chem., **143** (1871) 337.
- 5) P.H. Keck: Physica, **20** (1954) 1059.
- 6) D. Schwabe: Physicochem. Hydrodyn., **2** (1981) 263.
- 7) A. Cröll, Th. Kaiser, M. Schweizer, A.N. Danilewsky, S. Lauer, A. Tegetmeier and K.W. Benz: J. Cryst. Growth, **191** (1998) 365.
- 8) D. Schwabe, A. Scharmann, F. Preisser and R. Order: J. Cryst. Growth, **43** (1978) 305.
- 9) T. Yano, K. Nishino, S. Matsumoto, I. Ueno, A. Komiya, Y. Kamotani and N. Imaishi: Int. J. Microgravity Sci. Appl., **35** (2018) 35102.
- 10) T. Yano, K. Nishino, I. Ueno, S. Matsumoto, Y. Kamotani: Phys. Fluids, **29** (2017) 044105.
- 11) D. Schwabe and A. Scharmann: J. Cryst. Growth, **46** (1979) 125.
- 12) R. Rupp, G. Müller and G. Neumann: J. Cryst. Growth, **97** (1989) 34.
- 13) M. Wanschura, V.M. Shevtsova, H.C. Kuhlmann and H.J. Rath: Phys. Fluids, **7** (1995) 912.
- 14) D.E. Melnikov, V. Shevtsova, T. Yano and K. Nishino: Int. J. Heat Mass Transf., **87** (2015) 119.
- 15) M.K. Ermakov and M.S. Ermakova: J. Cryst. Growth, **266** (2004) 160.
- 16) K. Nishino, T. Yano, H. Kawamura, S. Matsumoto, I. Ueno and M.K. Ermakov: J. Cryst. Growth, **420** (2015) 57.
- 17) T. Yano, K. Nishino, S. Matsumoto, I. Ueno, A. Komiya, Y. Kamotani, and N. Imaishi: Microgravity Sci. Technol., **30** (2018) 599.
- 18) H.C. Kuhlmann, M. Lappa, D. Melnikov, R. Mukin, F.H. Mulddon, D. Pushkin, V. Shevtsova and I. Ueno: Fluid Dyn. Mater. Process., **10** (2014) 1.
- 19) V. Shevtsova, Y. Gaponenko, H.C. Kuhlmann, M. Lappa, M. Lukasser, S. Matsumoto, A. Mialdun, J.M. Montanero, K. Nishino and I. Ueno: Fluid Dyn. Mater. Process., **10** (2014) 197.
- 20) Shin-Etsu Chemical Co., Ltd.: Silicone fluid KF-96 performance test results, 1991.
- 21) T. Yano, K. Nishino, H. Kawamura, I. Ueno, S. Matsumoto, M. Ohnishi and M. Sakurai: Exp. Fluids, **53** (2012) 9.
- 22) M. Nishimura, I. Ueno, K. Nishino and H. Kawamura: Exp. Fluids, **38** (2005) 285.
- 23) K. Nishino, N. Kasagi and M. Hirata: J. Fluid Eng., **111** (1989) 384.
- 24) H.G. Maas, A. Gruen and D. Papantoniou: Exp. Fluids, **15** (1993) 133.
- 25) D.W. Marquardt: J. Soc. Ind. Appl. Math., **11** (1963) 431.
- 26) H.K. Yuen, J. Princen, J. Illingworth and J. Kittler: Img. Vis. Comput., **8** (1990) 71.
- 27) N. Shitomi, T. Yano and K. Nishino: Int. J. Heat Mass Transf., **133** (2019) 405.